

Nanoparticles

Electron-Beam-Induced Deposition of Bimetallic Nanostructures from Bulk Liquids**

Matthew Bresin, Adam Chamberlain, Eugeni U. Donev, Chandan B. Samantaray, Gregory S. Schardien, and J. Todd Hastings*

The fields of electron-beam-induced deposition (EBID) and pulse radiolysis have long been known to share a commonality where energetic particles, impinging on (or traversing through) condensed matter, cause chemical reactions in precursors. Further comparisons between these two techniques have been hampered as pulse radiolysis employs liquid-phase precursors, while EBID precursors are typically gases. Using a hybrid technique known as liquid-phase electron-beam-induced deposition (LP-EBID) we have investigated the application of well-known pulse radiolysis chemical kinetics to the LP-EBID process. We report that bimetallic deposits (AuAg and AuPt) produced with LP-EBID follow chemical kinetics found in pulse radiolysis studies, leading to predictable compositions. In addition, TEM results show the deposits are alloyed, consistent with high dose pulse radiolysis for similar materials.

While previous results in LP-EBID have shown the successful deposition of metal nanostructures with high purity,^[1–3] the chemical mechanism itself has received limited attention. It is likely that the mechanism shares similarities with both gas-phase EBID and pulse radiolysis. For instance, in pulse radiolysis,^[4] aqueous solutions containing metal ion complexes are exposed to high-energy electrons, ions, or photons with megaelectron volt energy, resulting in suspended or otherwise randomly distributed nanoparticles over a large irradiated area. In EBID^[5,6] the electron source is a relatively low-energy (keV) electron beam from a scanning electron microscope (SEM), allowing for site-specific patterning of nanoscale structures.

While the methodologies for producing nanoscale structures differ, both techniques are thought to induce chemical reactions through the generation of secondary species, such as the solvated electron in pulse radiolysis and secondary

electrons in EBID. Solvated electrons are well-known to act as reducing agents for the generation of metal clusters^[7,8] and to cause damage in biological specimens such as DNA.^[9] Similarly, secondary electrons with energies between 0–20 eV have been shown to bind to gas-phase EBID precursors, such as Pt(PF₃)₄^[10] and Co(CO)₃NO^[11] leading to molecular dissociation.

Since both pulse radiolysis and EBID have known mechanisms with secondary species, we hypothesize that similar mechanisms would be present in LP-EBID. As LP-EBID precursor solutions typically contain micro- to millimolar concentrations of ionic complexes, it is likely that primary electrons will react with H₂O molecules to produce various radicals, including solvated electrons, rather than reacting directly with the ionic complexes. Indeed, here we demonstrate that established rate constants of reactions between solvated electrons and metal ions can be applied to the resulting LP-EBID nanostructures, resulting in an excellent fit to multiple precursor concentrations for both AuAg and AuPt. These results show that LP-EBID bears a strong similarity to pulse radiolysis, and furthermore that extant literature can be applied to the site-specific deposition of high-purity materials.

In contrast to gas-phase EBID, liquid-phase experiments are most easily conducted on polyimide or silicon nitride membranes that serve to separate the solution from the vacuum of the electron-beam lithography system as illustrated in Figure 1 a. The electron beam energy is sufficient to penetrate the polyimide window and subsequently induce ion–electron reactions in the liquid reservoir. As depicted in the inset of Figure 1 a, deposition occurs on the liquid side of the polyimide window in proximity to the primary beam (additional details in the Supporting Information). Once the deposition process is complete, the top portion of the cell can be extracted for ex situ imaging. Figure 1 b–e show top-down dark-field scanning transmission electron microscope images of AuAg and AuPt deposits recorded by scanning electron microscopy (Quanta FEG, FEI, Hillsboro, OR USA). Figure 1 b and d demonstrate the site-specific deposition capabilities of LP-EBID, whereas Figures 1 c and e show the cluster or colloidal aspects of the deposits. For both AuAg and AuPt, the primary dot pattern is surrounded by varying levels of unintended, or collateral, deposition (additional discussion regarding the deposit morphology can be found in the Supporting Information). Figure 2 a shows nanoscale dots deposited from solutions containing varying concentrations of H₂AuCl₄ and H₂PtCl₆ acids. Figure 2 b shows similar results for mixtures of H₂AuCl₄ and AgNO₃. The deposits in Figure 2 a

[*] Dr. M. Bresin, A. Chamberlain, Dr. E. U. Donev, Dr. C. B. Samantaray, G. S. Schardien, Prof. Dr. J. T. Hastings
Department of Electrical and Computer Engineering
University of Kentucky
453 F. Paul Anderson Tower, Lexington, KY (USA)
E-mail: hastings@engr.uky.edu

[**] This material is partially based upon work supported by the Defense Advanced Research Projects Agency (DARPA) under award number N66001-09-1-2099. This material is also based upon work supported by the National Science Foundation under grant number CMMI-1125998. The authors thank C. May, B. Wajdyk, and the University of Kentucky Center for Nanoscale Science and Engineering as well as J. Ye, L. Rice, and the University of Kentucky Electron Microscopy Center for valuable technical support.



Supporting information for this article is available on the WWW under <http://dx.doi.org/10.1002/anie.201303740>.

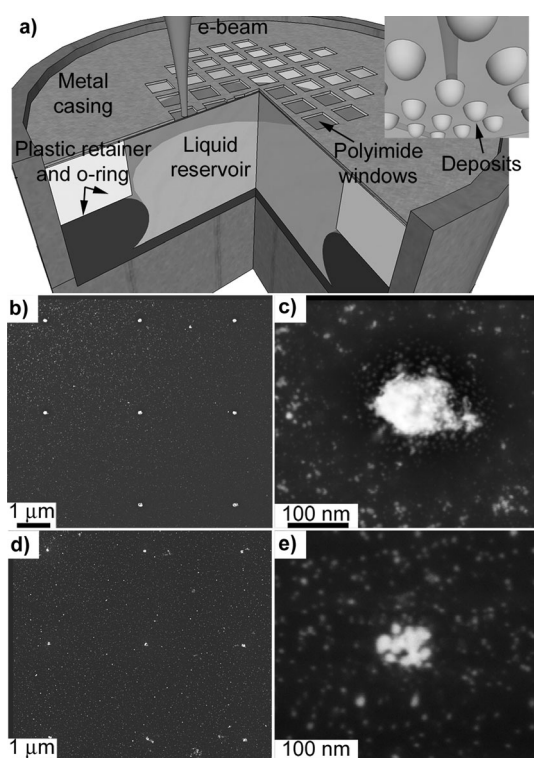
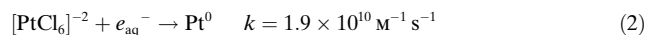
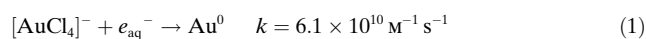


Figure 1. The liquid cell and examples of deposited patterns. a) Liquid precursors are contained within the sealed capsule and are accessible through an electron transparent polyimide membrane. Inset: The electron beam penetrates the thin polyimide membrane, inducing deposition on the liquid side. b) Ex situ (liquid side) dark-field scanning transmission electron micrograph (DF-STEM) of AuAg deposits produced with a dot dose of 60 pC. c) High-resolution image of an ex situ (liquid side) single deposit, showing partially imbedded colloidal AuAg particles. d) DF-STEM of AuPt deposits produced with a dot dose of 10 pC. e) High-resolution image of a colloidal AuPt deposit.

and b illustrate that arrayed nanoscale features are attainable at each solution concentration studied.

Perhaps the most intriguing aspect of this work is the clear relationship between deposit composition and solution composition. Figure 2c and d plot the fraction of the primary elements in the deposits (AuPt and AuAg, respectively) versus the concentration of the ion complexes in solution from Figure 2a and b. Values for the primary element composition are obtained from energy-dispersive X-ray (EDX) spectra, where the metal content fractions are simulated using the NIST DTSA-II software. Example fitting is shown in Figure 2e and f. Relative rate curves were produced by taking the limiting reaction rate and concentration ratio, $k_{M1}C_{M1}/(k_{M2}C_{M2})$. The predicted concentrations are based on the rate constant of the first reaction step between $[\text{AuCl}_4]^-$ or $[\text{PtCl}_6]^{2-}$ and a solvated electron, $e^-(\text{aq.})$, and do not contain any fitting parameters.

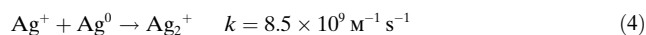
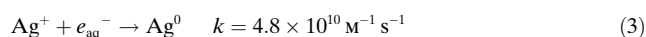
The overall reactions for Au and Pt, omitting several intermediate steps, and the measured rate constants for the first step taken from Ref. [8] are given in Equations (1) and (2).



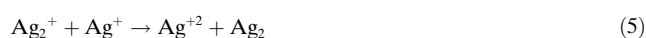
The excellent match between the predicted and experimental atomic fractions suggests that the first reaction step is rate-limiting for both elements.

Figure 2d shows a similar map between solution and deposit concentration for AuAg structures. In this case three reaction steps are required to produce stable metallic silver. In all cases we assume the precursor ion concentration, $[\text{Ag}^+]$, far exceeds that of the other reactants.

The first two reaction steps are given in Equations (3) and (4),^[12]



and the reaction is completed by Equation (5).^[13]



The rate constant of the first step is far faster than the second, and thus does not accurately predict the deposit composition. However, the rate constant for the second reaction step provides an excellent match to the experimental data, and appears to be the rate-limiting step.

These results are particularly exciting because they suggest that one may be able to identify rate-limiting reaction steps from available pulse radiolysis data and then predict the deposit composition for bimetallic electron-beam-induced deposition.

The deposit compositions were analyzed by EDX spectroscopy, and found to contain a combined metal composition typically exceeding 90 at.%. The primary contaminant for the AuPt structures is Cl, with a content of 9.4 ± 0.9 at.%. The contamination is presumably a result of byproducts from the chloroaurate and chloroplatinate ions. This is consistent with previous work on Au and Pt deposited separately.^[1,2] Likewise, the primary discernible contaminant in AuAg structures is also Cl with a content of 5.6 ± 0.8 at.%, again from $[\text{AuCl}_4]^-$. Oxygen, carbon, and nitrogen could conceivably be incorporated in the deposits from the environment; however, as these elements are present in the membrane, their respective concentrations in the deposit are difficult to assess.

In addition, we investigated the effects of dose on the composition. For example, reagents with faster reaction rates could conceivably be locally depleted at long deposition times (high dose) because of mass transport limitations. To test this possibility we acquired EDX spectra from 11 nanoparticles of 1:1 AuPt deposits exposed with doses between 12 and 132 pC (pC = picocoulomb). Variation in the Au:Pt ratio for these deposits is ± 3 at.%, which is within the error of the EDX measurement. Moreover, the maximum and minimum Pt concentrations occur at 108 and 48 pC, respectively, as opposed to the extremes of the dose range. Thus, over a practical dose range and within experimental error, we have not been able to discern a relationship between dose and deposit composition.

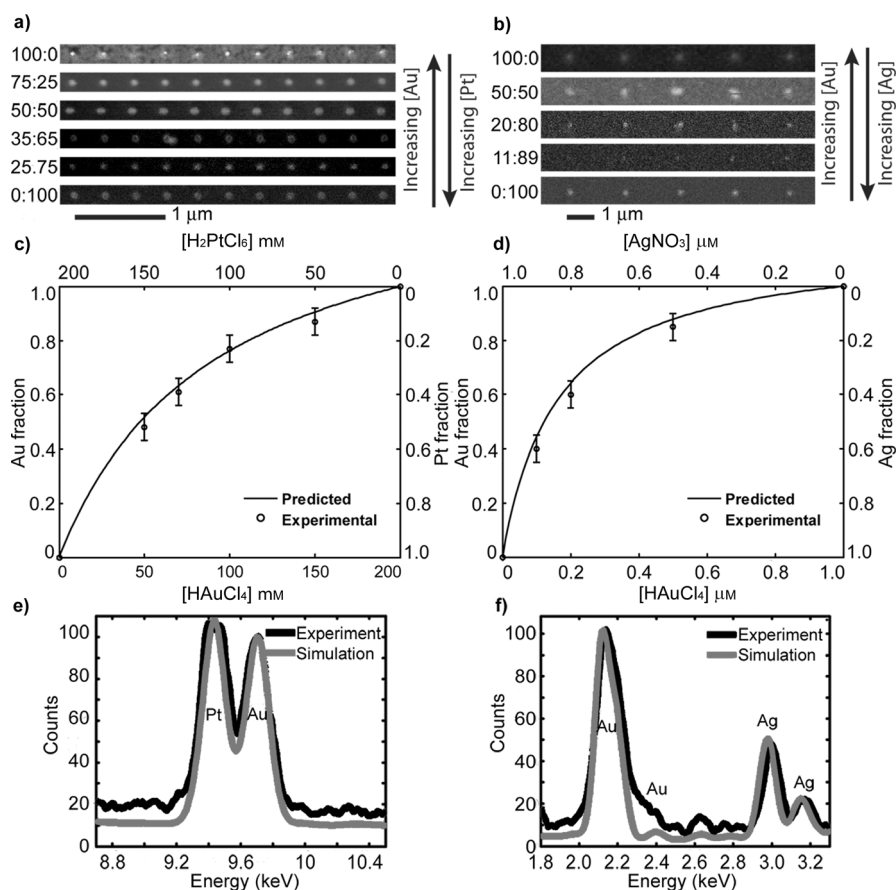


Figure 2. Predicted versus experimental composition of bimetallic deposits. a) AuPt patterns deposited from solutions of HAuCl_4 and H_2PtCl_6 with a total concentration of $200 \mu\text{M}$ and a dot dose of 100 pC . The solution concentration ratios are listed next to each set of deposits. b) AuAg patterns deposited from solutions of HAuCl_4 and AgNO_3 with a total concentration of 1 mM and a dot dose of 100 pC . c) Experimental data and relative rate curve [Eqs. (1) and (2)] for AuPt deposits. No fitting parameters are used in the predicted models. d) Experimental data and relative rate curve [Eqs. (1) and (4)] for AuAg deposits. e) Example EDX spectrum from a bimetallic AuPt deposit. The experimental data is well-matched by the simulated spectrum with a 50:50 Au:Pt ratio. The Au:Pt ratio in solution was 25:75. f) Example EDX spectrum from a bimetallic AuAg deposit. The experimental data is well-matched by the simulated spectrum with a 40:60 Au:Ag ratio. The Au:Ag ratio in solution was 10:90.

Treguer et al. have shown that pulse radiolysis of solutions containing Ag^+ and AuCl_4^- yielded either bilayer or alloy nanoparticles at lower (35 kGy h^{-1}) and higher ($7.9 \times 10^3 \text{ kGy h}^{-1}$) dose rates, respectively.^[7] At low-dose rates the silver atoms act as an electron relay for gold atoms, leading to the formation of gold core–silver shell particles. At high-dose rates, both Ag and Au atoms are fully reduced before subsequent electron transfer can occur, leading to alloy particles. We can place a conservative lower bound on the dose rate for our experiments by assuming that all of the primary electron energy is dissipated in a spherical volume with a diameter equal to the Bethe range of 20 keV electrons in water (see the Supporting Information for discussion). This yields a dose rate of approximately $2 \times 10^7 \text{ kGy h}^{-1}$. At these high-dose rates one would expect only alloy formation, which is consistent with TEM observations of the bimetallic deposits (micrographs and additional information are available in the Supporting Information).

field of radiation chemistry and the emergent area of electron-beam-induced processing.

Experimental Section

All deposition processes were conducted in a Raith e-LiNE electron beam lithography (EBL) system using a 20 keV electron beam and a beam current of 1.3 nA . Depositions were carried out on 150 nm thick polyimide membranes that form the top of commercial liquid electron-microscopy capsules (Quantomix, QX-102 WETSEM). The liquid cells contained $15 \mu\text{L}$ of precursor solution. Colloidal gold nanoparticles (about 50 nm in diameter) were placed on the vacuum side of the membrane to aid in focusing, while patterns were created on the bottom side of the membrane in contact with the precursor liquid. AuPt dots were patterned in arrays with doses ranging from 100 – 1100 pC per dot with periods of 350 nm . AuAg dots were patterned in arrays with doses ranging from 50 – 150 pC per dot with periods of $2 \mu\text{m}$. Finally, all the samples were rinsed with deionized water for several minutes and dried in air once they were removed

Bimetallic nanostructures are deposited here by simply mixing liquid precursors, where deposit composition can be predicted using established rate constants of reactions between solvated electrons and metal ions. In contrast, there are few examples of multi-element material deposition exist using EBID (with the recent exceptions of CoPt ^[14] and PtSi ^[15] deposition), because of the complexities in controlling injection, adsorption, and dissociation of multiple gas-phase precursors. In addition, the techniques and solutions described here are applicable to direct observation of crystal growth^[16] and liquid-phase imaging,^[17] while the nanostructures may have applications in fields such as patterned catalysis.^[18]

In conclusion, electron-beam-induced deposition from bulk liquids appears promising for patterning bimetallic nanostructures. Moreover, bimetallic structures appear to follow their single-element counterparts in terms of low-contamination levels. At experimentally preferable precursor concentrations and deposition doses, the deposit composition appears to be dose-independent within our current measurement capabilities. Finally, and most importantly, rate constants established over many years using pulsed radiolysis to study solvated electron–metal ion reactions can prove predictive of bimetallic deposit composition. These findings indicate that a more substantial intellectual bridge should be built between the long-standing

from the EBL chamber. Elemental analysis was conducted with energy-dispersive X-ray spectroscopy (Evex Si(Li)) in a Hitachi S-3200 SEM using a 20 keV primary beam and confirmed for one AuAg and one AuPt deposit in a JEOL-2010f TEM (Oxford Si(Li)) using a 200 keV primary beam. Monte Carlo simulation-based analysis using in NIST DTSA-II software package was used to quantify the deposit compositions. Error bounds on the deposit compositions were established by using a simulated 1:1 AuAg film as a baseline and taking the largest compositional deviation among simulations of 10 and 100 nm thick films both with and without infinite polyimide substrates. The resulting 10% relative error is consistent with conventional interpretation of standardless EDX analysis.

The precursor solutions were prepared in deionized water (18 M Ω) from H₂PtCl₆, HAuCl₄, and AgNO₃. All chemicals were obtained from Sigma-Aldrich and used as received. For the AuPt nanostructures total solute concentrations were fixed at 200 μ M while the individual precursor concentrations were varied between pure HAuCl₄ and pure H₂PtCl₆ as Au (200 μ M), Au (150 μ M) + Pt (50 μ M), Au (100 μ M) + Pt (100 μ M), Au (70 μ M) + Pt (130 μ M), Au (50 μ M) + Pt (150 μ M), and Pt (200 μ M). For the AuAg nanostructures the total solute concentration was fixed at 1 mM while the individual precursor concentrations varied between pure HAuCl₄ and pure AgNO₃ as Au (1.0 mM), Au(0.50 mM) + Ag (0.50 mM), Au (0.20 mM) + Ag (0.80 mM), Au(0.11 mM) + Ag (0.89 mM), and Ag (1.0 mM).

Received: May 2, 2013

Published online: June 20, 2013

Keywords: bimetallic nanostructures · electron-beam-induced deposition · nanoparticles · solvated electrons

- [1] G. Schardein, E. U. Donev, J. T. Hastings, *Nanotechnology* **2011**, *22*, 015301.

- [2] E. U. Donev, J. T. Hastings, *Nano Lett.* **2009**, *9*, 2715–2718.
 [3] L. E. Ocola, A. Joshi-Imre, C. Kessel, B. Chen, J. Park, D. Gosztola, R. Divan, *J. Vac. Sci. Technol. B* **2012**, *30*, 06FF08-07.
 [4] G. V. Buxton, Q. G. Mulazzani, A. B. Ross, *J. Phys. Chem.* **1995**, *24*, 1055–1349.
 [5] I. Utke, P. Hoffmann, J. Melngailis, *J. Vac. Sci. Technol. B* **2008**, *26*, 1197–1276.
 [6] I. Utke, A. Götzhäuser, *Angew. Chem.* **2010**, *122*, 9516–9518; *Angew. Chem. Int. Ed.* **2010**, *49*, 9328–9330.
 [7] M. Treguer, C. de Cointet, H. Remita, J. Khatouri, M. Mostafavi, J. Amblard, J. Belloni, R. de Keyzer, *J. Phys. Chem. B* **1998**, *102*, 4310–4321.
 [8] D. Behar, J. Rabani, *J. Phys. Chem. B* **2006**, *110*, 8750–8755.
 [9] E. Alizadeh, L. Sanche, *Chem. Rev.* **2012**, *112*, 5578–5602.
 [10] J. F. Friedman, T. M. Miller, J. K. Friedman-Schaffer, A. A. Viggiano, G. K. Rekha, A. E. Stevens, *J. Chem. Phys.* **2008**, *128*, 104303–104306.
 [11] S. Engmann, M. Stano, Š. Matejčík, O. Ingólfsson, *Angew. Chem.* **2011**, *123*, 9647–9649; *Angew. Chem. Int. Ed.* **2011**, *50*, 9475–9477.
 [12] E. Janata, A. Henglein, B. G. Ershov, *J. Phys. Chem.* **1994**, *98*, 10888–10890.
 [13] E. J. Hart, M. Anbar, *The hydrated electron*, Wiley-Interscience, New York, NY, **1970**, p. 122, and references therein.
 [14] F. Porrati, E. Begun, M. Winhold, H. S. Ch, R. Sachser, A. S. Frangakis, M. Huth, *Nanotechnology* **2012**, *23*, 185702.
 [15] M. Winhold, C. H. Schwalb, F. Porrati, R. Sachser, A. S. Frangakis, B. Kämpken, A. Terfort, N. Auner, M. Huth, *ACS Nano* **2011**, *5*, 9675–9681.
 [16] J. M. Yuk, J. Park, P. Ercius, K. Kim, D. J. Hellebusch, M. F. Crommie, J. Y. Lee, A. Zettl, A. P. Alivisatos, *Science* **2012**, *336*, 61–64.
 [17] N. de Jonge, F. M. Ross, *Nat. Nanotechnol.* **2011**, *6*, 695–704.
 [18] J.-U. Park, S. Nam, M.-S. Lee, C. M. Lieber, *Nat. Mater.* **2012**, *11*, 120–125.

Supporting Information

© Wiley-VCH 2013

69451 Weinheim, Germany

Electron-Beam-Induced Deposition of Bimetallic Nanostructures from Bulk Liquids**

*Matthew Bresin, Adam Chamberlain, Eugenio U. Donev, Chandan B. Samantaray, Gregory S. Schardien, and J. Todd Hastings**

anie_201303740_sm_miscellaneous_information.pdf

Table of Contents:

1) Notes on electron trajectories in Quantomix cells	1
2) TEM investigation of bimetallic nanoparticles	1-2
3) SEM images for deposit arrays	2-3

1 Notes on electron trajectories in Quantomix cells

As electrons travel through and interact with matter, they may undergo processes which change their direction and energy. Monte Carlo based simulations can be used to illustrate these processes. Using the Monte Carlo program CASINO,^[1] electron trajectories and energy distribution profiles can be plotted as shown in figure S1. Here the Quantomix cell is simulated as a 150 nm membrane of polyimide with the precursor solution comprised of H₂O. At the precursor concentrations used in this study the assumption of a majority H₂O bath solution is justified. The electron travel or ‘Bethe’ range found in our simulations is approximately 9.0 μm with a backscatter coefficient of 0.047. These values are generally consistent with experimental data acquired by Joy.^[2] Although the electrons may travel several microns into the precursor bath, the deposited energy is highly localized around the beam impact point.

In relation to the figure 1(a) inset, the beam easily traverses through the polyimide membrane, and in depositing significant energy near the membrane-liquid interface may explain why deposits form in the vicinity of the beam impact point. The minimum beam dose required to form a deposit depends heavily of the precursor solution constituents and their concentrations; however, deposits readily form between 10 – 50 pC per dot, and have been shown to form in the sub-pC range.^[3]

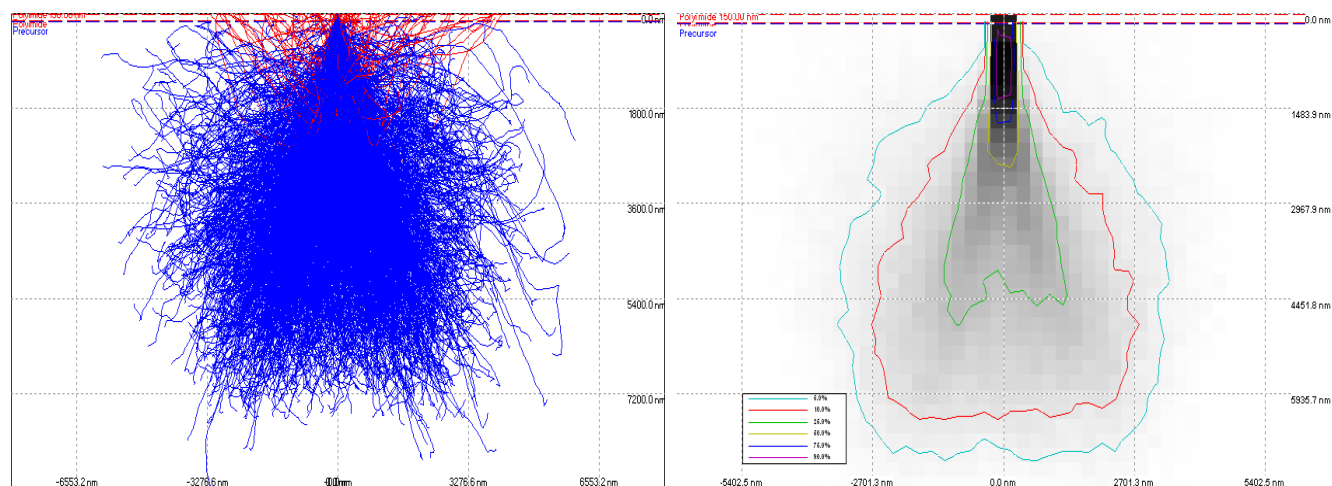


Figure S1. (Left) Electron trajectories in a Quantomix cell with a beam energy of 20 keV. (Right) Deposited energy, or energy transfer from primary electrons to the cell, as a function of depth.

2 SEM images for deposit arrays

The surrounding collateral deposition observed in figures 1(b) - 1(e) is represented by the small particulates surrounding the primary deposits. This deposition is generally undesirable in LP-EBID, but may prove useful for future attempts at localized ‘bulk’ fabrication of ultrasmall sub-10nm particles. This collateral deposition has been previously reported for e-beam induced deposition of Au from H₂AuCl₄ and can be minimized by adjusting the precursor concentration and deposition dose.^[4] The extent of collateral deposition appears to be composition dependent, and ultimately the deposition conditions may need to be optimized for a target material composition. For these experiments we maintained constant precursor concentrations and deposition conditions in order to better study the deposit composition; rather than optimize for minimal collateral deposition. The shadowing observed around the primary deposit shown in Figure 1(c) indicates etching, or dishing, of the polyimide substrate. This effect has also been observed previously and can be attributed to electron beam induced attack on the substrate.^[5]

The primary deposits shown in Figures 2(a) and 2(b) of the main text are typically < 100 nm diameter, but exhibit varying levels of compactness. The variance in compactness shows no clear trend in relation to solution composition, and may simply be a consequence of sample-to-sample differences in imaging conditions or variations in the polyimide film thickness. We

note that at other solution concentrations and dose conditions we have produced compact spheres, hemispheres, and wires of pure Pt,^[5] so the relationship between deposition conditions and deposit morphology requires additional study.

3 TEM investigation of bimetallic nanostructure

We investigated the nanostructure of the deposits using hi-resolution transmission electron microscopy (HRTEM). Figure S2 shows micrographs and Fourier transform insets of several nanocrystals of AuAg and AuPt deposits. The deposits are polycrystalline, comprised of approximately 5 nm diameter nanocrystallites, which is consistent with previous studies on gas phase EBID nanostructures.^[6] Fourier transforms taken from the AuAg deposits reveal that the overall structure is FCC with a contracted lattice parameter of 3.78 Å, similar to the 3.71 Å found in bimetallic nanoparticles produced by Kariuki *et al.*^[7] Additionally, there are several spots corresponding to mixed odd even reflections, shown in the Fourier transform inset of figure S2(a) and in figure S2(c), which are typically forbidden in an FCC structure. The presence of d_{110} and d_{210} reflections indicates a superlattice of an ordered alloy with A_3B structure.^[8,9]

AuPt alloys follow Vegard's law, where the lattice parameter of the alloy follows a linear weighted average of the elemental composition.^[10] In order to avoid possible confusion between the AuPt spacing and the Au/Pd coating, a standard reference (50 nm Au spheres) was employed for comparison against the AuPt real-space and diffraction images. Magnification and camera lengths were normalized, and multiple spot pairs were measured for the d_{111} reflections, resulting in a measured spacing of 2.35 ± 0.01 Å. A micrograph of the Au standard SAD pattern used as reference is shown in figure S2(d), where the spots measured are indicated by blue lines. Micrographs of real-space and SAD patterns for AuPt are shown as figures S2(b) and S2(e) respectively. The precursor solution used for the deposit in Figure S2(b) should nominally yield a 50:50 AuPt composition, resulting in a d_{111} lattice spacing of 2.31 Å. The measured d_{111} lattice spacing across several reflections is 2.30 ± 0.02 Å (red lines), consistent with alloys of 50 ± 10 at. % Au and Pt. The d_{200} spacing is verified in the diffraction pattern in figure S2(e) as 2.00 Å (green line), consistent with the alloy composition.

In order to prevent sample charging during TEM analysis, a light sputter coating of Au/Pd was employed. The Au/Pd contribution to the Fourier transforms and diffraction patterns where possible are indicated in the images to illustrate their separation from the alloyed deposits.

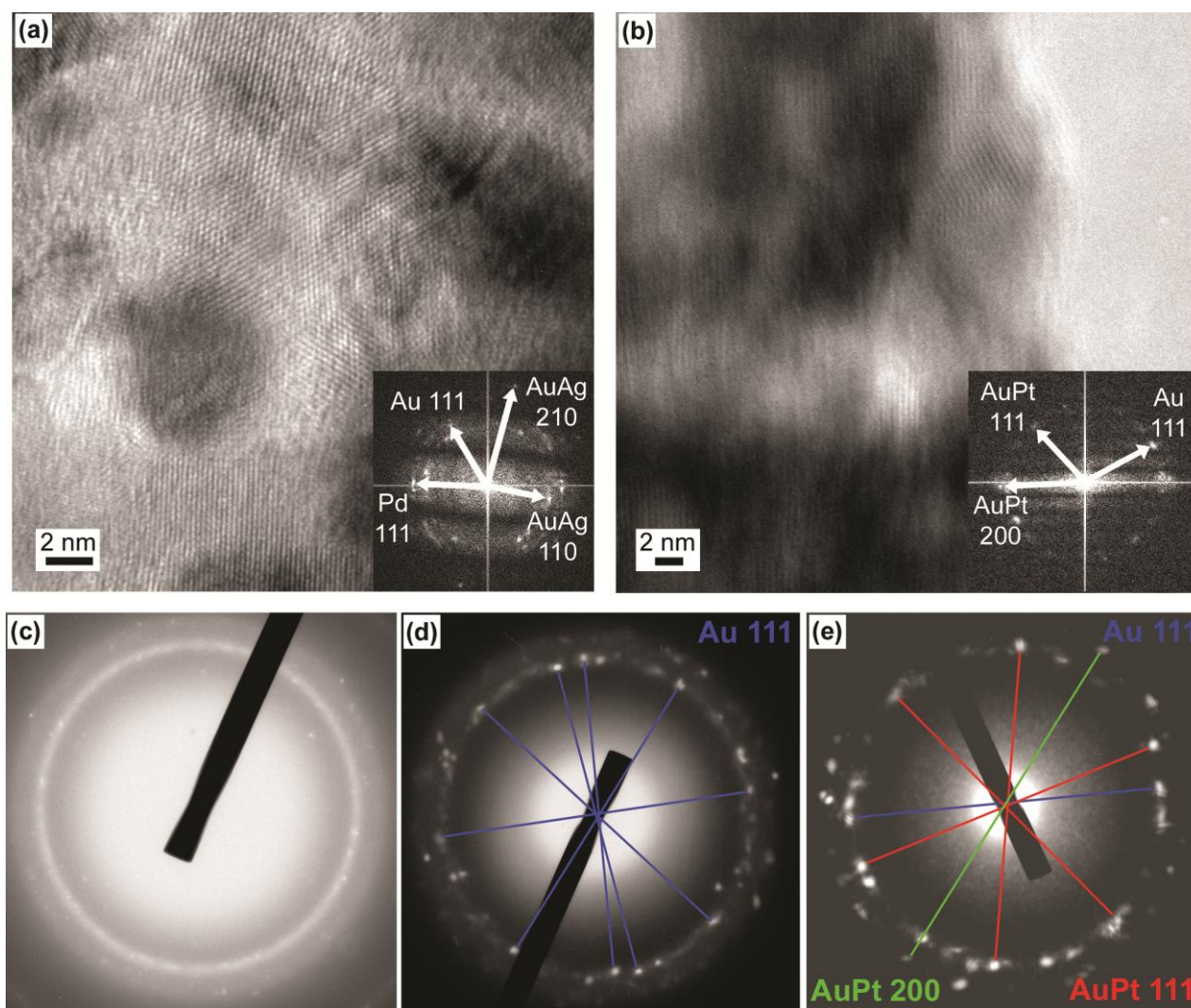


Figure S2. HRTEM of bimetallic nanocrystals. (a) Real space image and inset Fourier transform of an AuAg deposit, where the d_{110} and d_{210} reflections indicate an ordered A_3B alloy. Sputter coating with Au and Pd is used to mitigate charging and are marked in the inset for reference. (b) Real space and inset Fourier transform of an AuPt deposit with an average d_{111} spacing of 2.31 Å, consistent with a 50:50 Au:Pt alloy. (c) Selected area diffraction (SAD) pattern of an AuAg deposit array. (d) SAD pattern of 50 nm Au spheres. (e) SAD pattern of an AuPt deposition array, where assignments have been referenced to the Au standard in S2(d).

- [1] D. Drouin, A. R. Couture, D. Joly, X. Tastet, V. Aimez, R. Gauvin, *Scanning* **2007**, *29*, 92-101.
- [2] D. C. Joy, C. S. Joy, *J. Microsc.* **2006**, *221*, 84-88.
- [3] L. E. Ocola, A. Joshi-Imre, C. Kessel, B. Chen, J. Park, D. Gosztola, R. Divan, *J. Vac. Sci. Technol. B* **2012**, *30*, 06FF08-07.
- [4] G. Schardein, E. U. Donev, J. T. Hastings, *Nanotechnology* **2011**, *22*, 015301.
- [5] E. U. Donev, G. Schardein, J. C. Wright, J. T. Hastings, *Nanoscale* **2011**, *3*, 2709-2717.
- [6] J. Li, M. Toth, V. Tileli, K. A. Dunn, C. J. Lobo, B. L. Thiel, *Appl. Phys. Lett.* **2008**, *93*, 023130-023133.
- [7] N. N. Kariuki, J. Luo, M. M. Maye, S. A. Hassan, T. Menard, H. R. Naslund, Y. Lin, C. Wang, M. H. Engelhard, C.-J. Zhong, *Langmuir* **2004**, *20*, 11240-11246.
- [8] M. Treguer, C. de Cointet, H. Remita, J. Khatouri, M. Mostafavi, J. Amblard, J. Belloni, R. de Keyser, *J. Phys. Chem. B* **1998**, *102*, 4310-4321.
- [9] L. Reimer, H. Kohl, in *Transmission electron microscopy: Physics of Image Formation 5th Ed.*, Vol. 36 Springer, New York, NY **2008**, pp. 350-315.
- [10] G. De, C. N. R. Rao, *J. Mater. Chem.* **2005**, *15*, 891-894.